Nanoscale

Accepted Manuscript

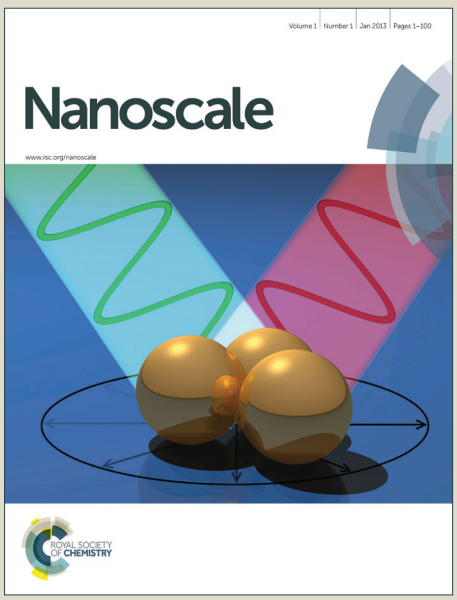

ROYAL SOCIETY OF CHEMISTRY

www.rsc.org/nanoscale

TITLE: Nickel doped cobalt ferrite nanoparticles: Efficient catalysts for the reduction of nitroaromatic compounds and photo-oxidative degradation of toxic dyes.

.

AUTHORS:

Charanjit Singh
Department of Chemistry,
Panjab University,
Chandigarh, India-160 014
chinu.thapar@gmail.com

Ankita Goyal
Department of Chemistry
Panjab University
Chandigarh, India- 160 014.
ankigoyal10@gmail.com

Sonal Singhal *
Assistant Professor,
Department of Chemistry,
Panjab University
Chandigarh, India- 160 014
sonal1174@gmail.com

CORRESPONDING AUTHOR: Sonal Singhal
Assistant Professor,
Department of Chemistry,
Panjab University,
Chandigarh, India - 160 014
Ph. No. +91-172-2534421(o)
+91-09872118810(m)
Fax No. +91-172-2545074
E-mail: sonal1174@gmail.com

Manuscript Contains:

Pages	**19**
Figures	**13**
Tables	**3**

Nickel doped cobalt ferrite nanoparticles: Efficient catalysts for the reduction of nitroaromatic compounds and photo-oxidative degradation of toxic dyes.

Charanjit Singh, Ankita Goyal and Sonal Singhal*
Department of Chemistry, Panjab University, Chandigarh, India-160014.
***sonal1174@gmail.com**

Abstract

This study deals with the exploration of $Ni_xCo_{1-x}Fe_2O_4$ (x = 0.0, 0.2, 0.4, 0.6, 0.8, 1.0) ferrite nanoparticles as catalysts for the reduction of 4-nitrophenol and photo-oxidative degradation of Rhodamine B. The ferrite samples with uniform size distribution were synthesized using the reverse micelle technique. The structural investigation was done using powder X-ray diffraction, high resolution transmission electron microscopy, energy dispersive X- ray and scanning tunneling microscopy. The spherical particles with ordered cubic spinel structure were found to have the crystallite size of 4–6 nm. Diffused UV-Visible reflectance spectroscopy was employed to investigate the optical properties of the synthesized ferrite nanoparticles. The surface area calculated using BET method was found to be highest for $Co_{0.4}Ni_{0.6}Fe_2O_4$ (154.02 m^2/gm). $Co_{0.4}Ni_{0.6}Fe_2O_4$ showed the best catalytic activity for the reduction of 4-nitrophenol to 4-aminophenol in the presence of $NaBH_4$ as reducing agent whereas $CoFe_2O_4$ was found to be catalytically inactive. The reduction reaction followed pseudo-first order kinetics. The effect of varying the concentration of catalyst and $NaBH_4$ on the reaction rates was also scrutinized. The photo-oxidative degradation of Rhodamine B, enhanced oxidation efficacy was observed with the introduction of Ni^{2+} in to the cobalt ferrite lattice due to octahedral site preference of Ni^{2+}. Almost 99 percent degradation was achieved in 20 min using $NiFe_2O_4$ nanoparticles as catalyst.

Keywords- Ni doped Cobalt ferrite; nitroaromatic compounds; catalytic reduction; Rhodamine B; photo-oxidative degradation.

1. Introduction

With the development of human era, massive urbanization led to the evolution of extensive industrialization and consequently large industrial contaminants mobilize to natural resources. These contaminants include the volatile organic compound (VOC), chlorinated solvents, fertilizers, dyes, phenols and nitroaromatic compounds.[1] Amongst these, the presence of toxic dyes and nitroaromatic compounds in wastewaters is of great concern as these are biologically and chemically stable, therefore it is difficult to remove them by natural degradation processes.[2,3] These contaminants are extensively present in the effluents from the pharmaceuticals, petrochemicals, pesticides and dying industries along with agricultural waste.[4] Such pollutants once released can cause various problems such as clogging the sewage treatment plants, adversely affecting aquatic biota and pose serious threats to human health. Nitroaromatic compounds, various dyes and their breakdown products are usually toxic and have carcinogenic and mutagenic effects towards biosphere.[5] The effective removal of these dangerous contaminants or their transformation in to some useful products before discharge is of utmost practical importance. Toxic dyes can be transformed in to H_2O and CO_2 using photocatalytic degradation. A simple and eco- friendly approach for the removal of nitro aromatic compounds is to transform them into valuable aromatic amines via catalytic reduction in the presence of $NaBH_4$ as reducing agent.[6] Aromatic amines are significant starting material for numerous biologically active and pharmaceutical compounds.[7]

There has been growing research efforts for the development of such catalysts which can assist in the treatment of wastewaters loaded with these harmful contaminants. So far a variety of

catalysts have been developed such as zeolites[8], BN nanofibres[9], expensive metal nanoparticles such as Au, Ag, Pt, Pd[10-14], metal oxides[15], ferrites[16], composite materials[17,18] etc. which are very effective for the removal of such contaminants. But the utilization of ferrites (metal oxides with iron as the major metallic component) as catalyst for the removal, degradation or transformation of such contaminants is one such practice, which is green, inexpensive, facile and widely applicable. Ferrites are stable, easy to synthesize, cost-effective, non-toxic, magnetically separable and reusable heterogeneous catalysts which are practically applicable for the treatment of wastewaters. The catalytic efficiency of ferrites is dependent upon the properties like cation distribution, porosity, particle size distribution, morphology and surface area which further depends upon the composition, synthetic procedure employed and the temperature at which ferrites have been annealed to achieve crystalinity.

Many research groups have employed ferrite nanoparticles as catalysts for the degradation of toxic dyes and for the reduction of nitroaromatic compounds. Lijun *et al.* synthesized $ZnFe_2O_4$ nanoparticles both in the presence succinic acid and in the absence of succinic acid. It was observed that the ferrite samlples synthesized in the presence of organic acid exhibited better visible-light photocatalytic activity towards Rhodamine B (RhB) degradation than that of the other.[19] Photocatalytic degradation of orange I azo dye was carried out by Borhan *et al.* in the presence of Al^{3+} doped zinc ferrite nanoparticles. Degradation efficiency was found to enhance with the introduction of Al^{3+} in to the zinc ferrite lattice and the sample in which Al^{3+} and Fe^{3+} were present in equi-molar amount was the best catalyst among the entire composition.[20] Photocatalytic ozonation of dyes was performed by Niyaz in the presence of copper ferrite nanoparticles as catalyst.[21] Feng *et al.* employed copper ferrite nanoparticles as catalyst for the reduction of 4-nitrophenol (4-NP) in the presence of $NaBH_4$ as

reducing agent. 95% conversion was achieved in 40 seconds.[22] Comparative catalytic efficiency of MFe_2O_4 (M= Cu, Ni and Zn) nanoferrites was evaluated for the reduction of nitrophenols (NP) in the presence of $NaBH_4$ as reducing agent. 50 equivalents of $NaBH_4$ was found to be the optimum amount and $CuFe_2O_4$ was observed to be the best catalyst among the synthesized pure ferrites.[23]

But a very few reports are available where ferrites have been explored as catalysts both for the oxidation and the reduction of organic pollutants. Also there is need for the development of such ferrites which have uniform size distribution, high surface area, high porosity and enhanced catalytic ability. Therefore, the present investigation deals with the synthesis of nickel doped cobalt ferrite nanoparticles ($Ni_xCo_{1-x}Fe_2O_4$ where, x = 0.0, 0.2, 0.4, 0.6, 0.8, 1.0) with controlled composition and size using the microemulsion method. The catalytic efficiency of the synthesized ferrite samples have been explored for the first time in the reduction of nitroaromatic compounds (4-NP as model compound) as well as for the photo-oxidative degradation of RhB dye. The detailed kinetic study for the reduction of 4-nitrophenol has been performed in the presence 50 and 25 equivalents of sodium borohydride. The comparative catalytic efficiency of the samples has been studied on the basis of surface area, cation distribution and optical properties.

2. Experimental

2.1. Materials

Cobalt chloride hexahydrate ($CoCl_2 \cdot 6H_2O$, 97%), nickel chloride ($NiCl_2$, 98%), ferric chloride ($FeCl_3$, 99.5%), sodium dodecyl sulfate (SDS, 90%), sodium hydroxide (NaOH, 98%), sodium borohydride ($NaBH_4$, 98%), sulphuric acid (H_2SO_4, 98%), hydrogen peroxide (H_2O_2,

30% w/v), hydrochloric acid (HCl, 37%) and Rhodamine B (99.7%) were purchased from Loba Chemicals and used without further purification. 4-nitrophenol (4-NP, 99%), absolute ethanol (C_2H_5OH, 99.9%), 1-butanol ($C_4H_{10}O$, 99.7%), ethyl acetate ($C_4H_8O_2$, 99.8%) and n-hexane (C_6H_{14}, 99.7%) were purchased from Fisher Scientific. Deionized water was obtained using an ultrafiltration system (Milli-Q, Milipore) with the measured conductivity of 35 mho cm^{-1} at 25 °C.

2.2. Physical measurements

The Infrared (IR) spectra for all the samples were recorded by FTIR instrument (PERKIN ELMER) using KBr pellets in the range 4000-400 cm^{-1}. Structural characterization of the samples was performed employing powder X-ray diffraction (XRD) technique using X-ray Diffractometer (PANanalytical) with CuKα radiation, High resolution transmission electron microscopy (HRTEM) and Energy dispersive X- ray (EDX) analysis using Hitachi (H7500) operated at 200 keV. Specific surface area was determined by N_2 adsorption method using single point surface area analyzer (SMARTSORB-93) after preheating the samples at 150 °C for 1 h. Optical properties were analyzed using the UV–VIS spectrophotometer (Analytikjena SPECORD-205). Photo-irradiation was carried out using 160 W mercury lamp (96000 Lux) with a distance of 6 inches between the light source and the target surface.

2.3. Fabrication of ferrite nanoparticles

Nickel doped cobalt ferrite nanoparticles were synthesized using reverse micelle method as shown in Fig. 1. [24] In a typical synthesis, two stable reverse micellar microemulsion systems with identical weight ratios of the four basic constitutive components: sodium dodecyl sulphate, 1-butanol, n-hexane and water (3.03: 5.57: 1.64: 89.82) were prepared. To one system metal

salts- ferric chloride, nickel chloride and cobalt chloride were added in stoichiometric amounts and subjected to sonication for half an hour. To second microemulsion 20 mL of 5 M NaOH was added, which served as a precipitating agent. The two microemulsions were mixed and stirred vigrously for an hour in air at room temperature. The as-synthesized solid hydroxide precursor was filtered after washing several times with absolute ethanol. The filtered product was dried in an oven at 110 $^{\circ}$C. Finally, the $Co_{1-x}Ni_xFe_2O_4$ nanospheres were obtained by annealing of the precursor at 400 $^{\circ}$C for 5 hours.

2.4. Catalytic and photocatalytic activity measurements

Reduction of 4-NP was carried out using $NaBH_4$ as reducing agent in aqueous medium The reaction was carried out at room temperature. For the reduction reaction 20 mL of 0.036 M aqueous solution of 4-NP was taken and 1.37 g (50 equivalents) of $NaBH_4$ was added. The reaction mixture was subjected to constant stirring. With the addition of $NaBH_4$, the color of the solution instantly turned to dark yellow, indicating the formation of phenolate ion. After 1 minute desired amount of $Ni_xCo_{1-x}Fe_2O_4$ (x = 0.0, 0.2, 0.4, 0.6, 0.8, 1.0) catalyst was added and stirring was continued. As the time elapsed visual change in solution colour from dark yellow to grey was observed, demonstrating the reduction of 4-NP. The reaction progress was checked by withdrawing 100 µL aliquots from the reaction mixture at regular time intervals, quenched by adding 5 mL of 2 M HCl and recording the UV-Visible spectrum. Attenuation of the absorbance peak at 317 nm of the reactant NP and appearance of a new peak at 268 nm confirmed the formation of 4-aminophenol (4-AP). After the completion of reaction, the catalyst was magnetically recovered using an external magnet followed by the addition of ammonium chloride to neutralize the excess of $NaBH_4$. Finally the product was extracted out of the aqueous solution with ethyl acetate and evaporated under vacuum to obtain the dried product.

The photo-oxidative degradation of RhB was performed under visible light irradiation (160 W mercury lamp with 96000 Lux intensity with a distance of 6 inches between the light source and the target surface). For a typical photocatalytic reaction, 50 mg of catalyst was dispersed in 100 mL of 50μM aqueous solution of RhB and pH of solution was set at 2 using dilute sulphuric acid. Before irradiation, the solution was stirred in dark for 30 min to establish adsorption/desorption equilibrium between the catalyst and dye solution. Thereafter, 100 μL of 30 % H_2O_2 was added and the solution was exposed to visible light with constant stirring. 2 mL aliquots were drawn out at set time intervals and the catalyst was filtered off using syringe filter. The change in concentration of the degraded dye solution was determined with the help of UV-Visible spectroscopy.

3. Results and discussion

3.1. Fourier transform infra-red (FT-IR) spectroscopy

In the FT-IR spectra of ferrites two peaks are generally observed, corresponding to the M-O bond in the octahedral and the tetrahedral sites of the ferrite sub-lattice.[25] FT-IR spectra were recorded for all the samples annealed at 400 °C. Variation in infra-red frequency bands, corresponding to the M-O bond in the octahedral and the tetrahedral sites, with change in composition for $Ni_xCo_{1-x}Fe_2O_4$ (x= 0.0, 0.2, 0.4, 0.6, 0.8, 1.0) is shown in Fig. 2. Lower frequency band at ~ 415 cm^{-1} is assigned to the stretching mode of the M-O bond in the octahedral sites whereas, higher frequency band at ~560 cm^{-1} is attributed to the stretching vibrations of the M-O clusters in the tetrahedral sites.[26]

3.2. Powder X-ray Diffraction (XRD) studies

Powder XRD allows for rapid and non-destructive analysis of multi-component mixtures without the need for extensive sample preparation. Fig. 3 shows the XRD patterns of $Ni_xCo_{1-x}Fe_2O_4$ (x = 0.0, 0.2, 0.4, 0.6, 0.8 and 1.0) nanoparticles annealed at 400 °C. All the peaks could be indexed to the (2 2 0), (3 1 1), (4 0 0), (4 4 0) and (5 1 1) lattice planes of the cubic unit cell indicating the formation of single phase with Fd-3m space group (JCPDS 22-1012). Broad peaks were observed in all the samples demonstrating the lower degree of crystallization at lower annealing temperatures. Crystallite size was calculated from the line broadening of the most intense (3 1 1) peak using the classical Scherrer equation.[27]

$$d = 0.9\lambda/ \beta \cos\theta$$

where d is the average crystallite size, β is the full width at half maximum (FWHM), λ is the X-Ray wavelength (1.542 A°) and θ is the angle of diffraction. The crystallite sizes for all the $Ni_xCo_{1-x}Fe_2O_4$ ferrite nanoparticles were found to be in the range of 4 - 6 nm. Powley and Le bail refinement methods were employed to calculate the dimensional changes in the lattice parameter with increasing Ni content in $Ni_xCo_{1-x}Fe_2O_4$ nanoparticles. The values of lattice parameter, 8.33 A° for $NiFe_2O_4$ and 8.38 A° for $CoFe_2O_4$, were in good agreement with literature.[28,29] With increase in Ni content the lattice parameter value was found to decrease. This could be attributed to the fact that Ni^{2+} (with smaller radii i.e Tet: 0.55 A°, Oct: 0.69 A°) replaced Co^{2+} (with larger radii i.e Tet: 0.58 A°, Oct: 0.745 A°) which led to the contraction of the unit cell.[30] X-ray density was also calculated for $Ni_xCo_{1-x}Fe_2O_4$ nanoparticles according to the relation:

$$d_x = 8M/Na^3$$

where 'M' is the molecular mass, 'N' is the Avogadro's number and 'a^3' is the volume of the cubic unit cell. The value of X-ray density increased linearly with increasing Ni content. The values of crystallite size, lattice parameters and X-ray densities are given in Table. 1.

3.3 HRTEM and EDX characterization

Shape, size, crystallinity, lattice interplaner distance and elemental composition were examined using HRTEM and EDX characterization techniques. Prior to analysis, annealed samples were dispersed in ethanol and sonicated for an hour to obtain a clear dispersion. Fig. 4(a) clearly shows the lattice interplanar distance, which indicates that ultrafine particles were well crystallized in to single crystals. The interplanar distance completely agreed with (4 0 0), (3 1 1), (2 2 0) and (1 1 1) planes of the $NiFe_2O_4$ nanostructures.[31] The average fringe width of 0.21, 0.26, 0.29 and 0.47 nm was calculated by profile of frame at different portions of image as shown in Fig. 4(b). No secondary phase was detected by HRTEM which was in good agreement with XRD results. Selected area electron diffraction (SAED) patterns (Fig. 4(c)) revealed good crystallinity with a set of strong diffraction rings which were all aligned with the XRD peaks. Fig. 4(d) shows the HRTEM image of $NiFe_2O_4$ nanoparticles which indicates that the spherical shaped particles were well estranged with diameter of around 3 nm. EDX spectrum shown in Fig. 4(e) confirmed the composition of sample to be Ni: Fe: O = 1:2:4. The signals corresponding to Cu and C were due to copper grid. A negligibly small peak of sulphur (~ 0.64%) was also observed which could be due to the surfactant used in the synthesis. The typical structural data for $CoFe_2O_4$ and $Co_{0.4}Ni_{0.6}Fe_2O_4$ nanoparticles are shown in Fig. 5. No change in the interlayer distance between the cobalt ferrite and the nickel doped cobalt ferrite samples was observed. Fig. 6 shows the variation of shape and size distribution with the nickel ion doping in cobalt ferrite lattice. Fig. 6(a) and 6(b) divulges the approximate spherical shape of cobalt ferrite

with particles size of around 7-8 nm. Clean surface with well-defined wall boundaries revealed that there was no agglomeration in the cobalt ferrite samples. Decrease in the particle size with small variation in the size distribution was observed with Ni^{2+} doping. Particle size of around 3-6 nm was observed for $Co_{0.4}Ni_{0.6}Fe_2O_4$ sample (Fig. 6(c) and 6(d)). $NiFe_2O_4$ nanoparticles were observed to have particle size of around 3 nm with similar size distribution (Fig. 6(e) and 6(f)).

3.4. Scanning tunneling microscopy (STM) and Raman spectroscopy

STM technique is used for imaging surfaces at atomic level and provides information about the 3-D structure. Fig. 7(a) shows the typical STM image of $Co_{0.4}Ni_{0.6}Fe_2O_4$ ferrite. Ferrite samples were observed to be highly porous. Fig. 7(b) portrays the typical raman spectrum of $Co_{0.4}Ni_{0.6}Fe_2O_4$ ferrite. Raman peaks in the range of 460-660 cm^{-1} and 660-720 cm^{-1} represents the octahedral and tetrahedral vibrational modes respectively.[32] Fundamental scattering peaks at 320, 473 and 660 cm^{-1} corresponding to Fe^{2+}, Ni^{2+} and Co^{2+} cations present in the lattice were observed.

3.5. *BET Surface area analysis*

The surface area of $Ni_xCo_{1-x}Fe_2O_4$ (x = 0.0, 0.2, 0.4, 0.6, 0.8 and 1.0) nanoparticles was measured using the BET method. The samples were preheated at 150 °C for 1 hour before N_2 adsorption. With the introduction of Ni^{2+} in to the cobalt ferrite lattice significant increase in surface area was observed. Surface area values for $Ni_xCo_{1-x}Fe_2O_4$ (x = 0.0, 0.2, 0.4, 0.6, 0.8 and 1.0) came out to be 44.38, 80.29, 112.06, 154.02, 135.88 and 141.41 m^2/gm respectively. $Ni_{0.6}Co_{0.4}Fe_2O_4$ ferrite was observed to have the highest surface area among all the samples.

3.6. Optical properties

Diffused reflectance (DR) UV-Visible spectroscopy was used to investigate the optical properties of the synthesized ferrite nanoparticles. Band edge absorption spectra for the entire ferrite composition are shown in Fig. 8. Absorbance in the range 670-1080 nm covers the visible region which is significant for photocatalytic reactions. Band edge absorption onset for cobalt ferrite was observed at 1080 nm and with increase in Ni^{2+} doping the edge absorption value sequentially decreased up to x= 0.6 and then increased. Band edge absorption values for $Ni_xCo_{1-x}Fe_2O_4$ (x = 0.2, 0.4, 0.6, 0.8 and 1.0) were 973, 899, 764, 778 and 824 nm respectively. The optical absorption coefficient near the band edge follows the equation[33]:

$$\alpha h\nu = A(h\nu - E_g)^{1/2}$$

where α, h, ν, E_g, and A are the absorption coefficient, Plank's constant, light frequency, band gap, and proportionality constant respectively. The band gap energy values were estimated from the plot of $(\alpha h\nu)^2$ versus photon energy (hν) as shown in Fig. 9. The calculation of the band gap energy involves the extrapolation of linear part of the curve obtained by plotting $(\alpha h\nu)^2$ vs hν to cut the energy axis. The estimated band gap values were found to be 1.14, 1.27, 1.38, 1.62, 1.59 and 1.51 eV for x = 0.0, 0.2, 0.4, 0.6, 0.8 and 1.0 respectively. Considerable change in the band gap values was observed with Ni^{2+} doping. A red shift from the band gap values for nickel and Cobalt ferrite (2.2 and 1.45 eV) was observed which might be due to defects and the sub-band-gap energy level formation in the nanoparticles.[34]

3.7. Catalytic studies

3.7.1. Reduction of 4-NP

Catalytic reduction of 4-NP to 4-AP in the presence of $NaBH_4$ as reducing agent, was chosen as the model reaction for the conversion of nitroaromatic compounds to aromatic amines. Reduction of 4-NP has also been employed before for evaluating the catalytic performance of noble-metal nanoparticles.[35-38] This reaction can be easily monitored by using UV-Visible spectroscopy because 4-NP in the acidic media absorbs at 317 nm whereas 4-AP absorbs at 268 nm. In the catalyzed reaction, a gradual decrease in the nitrophenol peak and the emergence of the aminophenol peak was observed, which confirmed the occurrence of reduction.

3.7.1.1. UV-Visible spectroscopy and catalytic activity of $Ni_xCo_{1-x}Fe_2O_4$

The reaction progress for the conversion of 4-NP to 4-AP was studied using the UV-Visible spectroscopy. 4-NP shows absorption peak at 317 nm which experienced a blue shift to 400 nm when $NaBH_4$ was added indicating the formation of phenolate ion.[39] The reaction started right away with the addition of catalyst. Sample aliquots were withdrawn from the reaction mixture at fixed time intervals, followed by the addition of HCl. HCl was added to quench the reaction. With the addition of HCl, the absorption maxima relapsed to 317 nm corresponding to 4-NP. In the successive readings the intensity of absorption peak at 317 nm decreased gradually and emergence of new peak at 268 nm was observed indicating the conversion of 4-NP to 4-AP. 4-AP absorbs at 300 nm in the UV-Visible spectrum. Shift in the absorption peak from 300 nm to 268 nm was observed due to the presence of HCl which converted 4-AP to 4-aminophenol hydrochloride.[39]

The reduction reactions were performed with 50 equivalents of $NaBH_4$ and $Ni_xCo_{1-x}Fe_2O_4$ (x = 0.0, 0.2, 0.4, 0.6, 0.8 and 1.0) nanoparticles as catalyst. $CoFe_2O_4$ was inactive for the reduction and with the introduction of Ni^{2+} in to the cobalt ferrite lattice the catalytic efficiency was dramatically enhanced. Fig. 10 shows the UV-Visible spectra for the reduction of 4-NP in

the presence of 50 equivalents of $NaBH_4$ and 30 mole % of catalyst. The effect of the concentration of catalyst was also studied by carrying out the reduction reactions in the presence of varying amounts (5 mole %, 10 mole % and 30 mole %) of catalysts ($Ni_xCo_{1-x}Fe_2O_4$ (x = 0.0, 0.2, 0.4, 0.6, 0.8 and 1.0)). It was observed that the catalytic efficacy increased with increase in the amount of catalyst.

In order to investigate the viability of reaction at low concentration of $NaBH_4$, the amount of $NaBH_4$ was decreased from 50 to 25 equivalents and the reduction reactions were performed using 30 mole % of catalysts which led to increase in the reaction times. However, the catalysts were still active at such low concentration of $NaBH_4$ (Fig. 11), which entailed the economic and cost efficient eminence of the reaction. An initial delay in catalytic reaction was observed, which could be due to oxidized metallic surface, the reduction of dissolved oxygen in solution or unavailability of the active metal at the octahedral reaction site.[40]

3.7.1.2. Chemical kinetics

As the concentration of $NaBH_4$ is in excess, the reduction reaction could be considered to follow pseudo first order kinetics. Pseudo first order rate constants could be calculated by employing the following rate law equation:

$$\ln(A_t/A_o) = - K_{app}t$$

where, A_t is the absorbance at any time t, A_0 is the absorbance at time t=0. The plots of $\ln(A_t/A_o)$ vs time (t) for the reduction of 4-NP in the presence of 25 and 50 equivalents of $NaBH_4$ with varying amounts (5 mole %, 10 mole % and 30 mole %) of $Ni_xCo_{1-x}Fe_2O_4$ (x = 0.2, 0.4, 0.6, 0.8 and 1.0) catalyst are shown in Fig. 12. Rate constant values calculated from the slope of straight line obtained from the plot of $\ln(A_t/A_o)$ vs time (t) are given in Table. 3. Greater the rate

constant value higher was the activity of the catalyst. Rate constant values for 30 mole % of $NiFe_2O_4$ and $Ni_{0.6}Co_{0.4}Fe_2O_4$ nanoparticles were found to be 9.9 and 10.3 min^{-1} respectively. The rate constant values in the present work were very high as compared other catalysts reported earlier.[4,5,23,39,41]

3.7.1.3. Catalytic ability of $Ni_xCo_{1-x}Fe_2O_4$ (x = 0.0, 0.2, 0.4, 0.6, 0.8 and 1.0)

Substantial augmentation in the catalytic ability was observed with Ni^{2+} doping in to the cobalt ferrite lattice. $CoFe_2O_4$ nanoparticles were found to be inactive for the reduction of 4-NP. This was confirmed from the fact that no change in the absorption maxima of 4-NP was noticed even when the reaction was studied for 5 hours. In the presence of 50 equivalents of $NaBH_4$ and 30 mole % of $Ni_xCo_{1-x}Fe_2O_4$ (x = 0.2, 0.4) nearly 99% conversion was achieved in 6 and 2 minutes respectively and with $NiFe_2O_4$ and $Ni_{0.6}Co_{0.4}Fe_2O_4$ as catalysts complete conversion was achieved within 30 seconds. In the presence of 25 equivalents of $NaBH_4$ and 30 mole % of $Ni_{0.6}Co_{0.4}Fe_2O_4$ catalyst complete conversion was achieved within 20 minutes The completion times for the reaction in the presence of 25 and 50 equivalents of $NaBH_4$ and varying amounts of $Ni_xCo_{1-x}Fe_2O_4$ (x = 0.0, 0.2, 0.4, 0.6, 0.8 and 1.0) catalysts are given in Table. 2.

The enhancement of catalytic activity with the introduction of Ni^{2+} in to the cobalt ferrite lattice could be due to their octahedral site preference.[23] The octahedral sites are exposed on the surface. So the metal ions present at the octahedral sites play a crucial role for the catalytic reactions. Octahedral sites of the cubic crystal structure act as a medium to transfer electrons from BH_4^- to 4-NP which leads to the formation of 4-AP.[40] Considering this factor, the catalytic activity of $NiFe_2O_4$ should be highest. The BET surface area and TEM studies depicted extremely small particle size and maximum surface area (154.02 m^2/gm) for $Ni_{0.6}Co_{0.4}Fe_2O_4$ nanoparticles. So bearing in mind both the factors the highest catalytic activity was observed for

$Ni_{0.6}Co_{0.4}Fe_2O_4$ followed by $NiFe_2O_4$ which was in good agreement with the experimental results.

3.7.2. Photo-degradation of RhB

Photocatalytic activity of nickel doped cobalt ferrite nanoparticles was evaluated by carrying out the photo-oxidative degradation of RhB. For the photocatalytic experiment catalyst was dispersed in the dye solution, followed by stirring under dark to attain adsorption/desorption equilibrium, then the pH was adjusted to 2 and then the solution was kept under visible light. Presence of light, ferrite, H_2O_2 and acidic pH were necessary to generate heterogeneous photo-fenton reagent for the degradation of dye to occur. Control experiments were performed so to understand the role of H_2O_2 in the presence and absence of catalyst for the degradation of dye.

3.7.2.1. UV-Visible spectroscopy and catalytic activity of $Ni_xCo_{1-x}Fe_2O_4$

Characteristic peak of RhB is observed at 556 nm in the UV-Visible spectrum. The peak at 556 nm diminished with time time without the appearance of any new band in the UV or visible region and the solution became colourless indicating the complete degradation of dye. The degradation percentage was calculated by applying following equation[38]:

$$Degradation\ percentage = \frac{A_0 - A_t}{A_0} \times 100$$

where A_o is initial absorption intensity of dye and A_t is the absorption intensity at time t. The plots of degradation percentage vs time for the entire ferrite composition are given in Fig. 13. To explore the role of H_2O_2 in the photocatalytic degradation of dye control experiments were performed and 39 percent dye was observed to degrade in 90 minutes when reaction was performed in the absence of catalyst and just 5 percent degradation was there in the presence of $NiFe_2O_4$ nanoparticles without H_2O_2. This could be due to attenuation in the generation of

hydroxyl radicals in the absence of catalyst and vice-versa. 97 percent degradation was achieved in 90 minutes when cobalt ferrite was used as catalyst in the presence of H_2O_2. Drastic decrease in degradation time was observed when Ni^{2+} doped cobalt ferrites were used as catalyst.

3.7.2.2. Catalytic ability of $Ni_xCo_{1-x}Fe_2O_4$ (x = 0.0, 0.2, 0.4, 0.6, 0.8 and 1.0)

Dramatic change in the degradation time with the introduction of Ni^{2+} in to the cobalt ferrite lattice could be related to the optical behavior and and octahedral site preference of Ni^{2+}. With nickel doped cobalt ferrite nanoparticles complete degradation was achieve in 20-25 minutes with slight difference in their catalytic activity whereas, with cobalt ferrite nanoparticles complete degradation occurred in 90 minutes. This could be due to the reason that Ni^{2+} seek to the octahedral site and replace the cobalt ions which were catalytically less active thereby, increasing catalytic activity. Also large band gap energy values inhibit the recombination of photo-generated charge carriers.[42] As discussed earlier, with Ni doping band gap increased, the recombination of electron and hole became difficult and electrons were available for oxidation, leading to attenuation of degradation time durations.

Conclusions

This is the first ever report where Ni doped cobalt ferrite nanoparticles synthesized using the reverse micelle technique were discovered as efficient catalysts both for the photo-oxidative degradation as well as for the reduction of nitroaromatic compounds. Reduction of 4-NP and photo-oxidative degradation of RhB were chosen as the model reactions to explore the catalytic efficiency. It was observed that with the introduction of Ni^{2+} in to the cobalt ferrite lattice the reducing as well as the oxidizing abilities enhanced spectacularly. $NiFe_2O_4$ nanopaticles were found to have the smallest particle size of ~3 nm. $Ni_{0.6}Co_{0.4}Fe_2O_4$ nanoparticles were observed to have highest surface area followed by $NiFe_2O_4$. $Ni_{0.6}Co_{0.4}Fe_2O_4$ and $NiFe_2O_4$ were observed to

be the best catalyst for the reduction of 4-NP and for the photo-oxidative degradation of RhB respectively. In comparison with other nanocatalysts reported in literature, $Ni_xCo_{1-x}Fe_2O_4$ (x = 0.2, 0.4, 0.6, 0.8 and 1.0) nanocatalysts offers several advantages. Since Ni doped cobalt ferrites are magnetic, they can be readily separated from the reation mixture without filtering. The recyclability of the nanocatalyst is economically important in industry. The synthesized nanocatalysts were stable, recyclable and showed excellent catalytic activity. Furthermore, Ni doped cobalt ferrite nanoparticles allows the treatment of toxic dyes and organic pollutants laden wastewaters in industry.

Acknowledgements

The authors are highly grateful to the DST (SERB) and Council of Scientific and Industrial Research (CSIR) for providing the necessary financial support.

References

1. Y. I. M. Meytal and M. Sheintuch, *Ind. Eng. Chem. Res.*, 1998, **37**, 309-326.
2. R. Dai, J. Chen, J. Lin, S. Xia, S. Chen and Y. Deng, *J. Hazard. Mater*., 2009, **170**, 141–143.
3. S. F. Nishino, J. C. Spain, Z. He, J. C. Spain, J. B. Hughes and H. J. Knackmuss, (Eds.), Lewis Publ., New York, pp. 7-61.K.
4. K. Layek, M. L. Kantam, M. Shirai, D. N. Hamane, T. Sasaki and H. Maheswaran, *Green Chem.*, 2012, **14**, 3164-3174.
5. J. R. Chiou, B. H. Lai, K. C. Hsu and D. H. Chen, *J. Hazard. Mater.*, 2013, **248–249**, 394-400.
6. T. R. Mandlimath and B. Gopal, *J. Mol. Catal. A: Chem*.,2011, **350**,9-15.
7. S. M. Abdallah, G. G. Mohamed, M. A. Zayed, M. S. A. El-Ela, *SpectrochimActa A*., 2009, **73,** 833-840.
8. J. Xie, W. Meng, D. Wu, Z. Zhang and H. Kong, *J. Hazard. Mater.*, 2012, **231– 232**, 57-63.
9. L. Xue, B. Lu, Z. S. Wu, C. Ge, P. Wang, R. Zhang and Z. D. Zhang, *Chem. Eng. J.*, 2014, **243**, 494–499.
10. N. Pradhan, A. Pal and T. Pal, *Colloids Surf. A*., 2002, **196**, 247-257.
11. L. Ai and J. Jiang, *Bioresour. Technol.*, 2013, **132**, 374-377.
12. Y. C. Chang and D. H. Chen, *J. Hazard. Mater*., 2009, **165**, 664-669.
13. H. Koga and T. Kitaoka, *Chem. Eng. J*., 2011,**168**, 420-425.
14. W. Zhang, F. Tan, W. Wang, X. Qiu, X. Qiau and J. Chen, *J. Hazard. Mater.*, 2012, **217-218**, 36-42.
15. Y. C. Chang and D. H. Chen, *J. Hazard. Mater.*, 2009,**165**,664-669.
16. J. Feng, L. Sua, Y. Ma, C. Ren, Q. Guo and X. Chen, *Chem. Eng. J*., 2013, **221**, 16–24.
17. P. Yang, A. D. Xu, J. Xia, J. He, H. L. Xing, X. M. Zhang, S. Y. Wei and N.N. Wang, *Appl. Catal. A*., 2013, **470**, 89-96.

18. V. K. Gupta, N. Atar, M. L.Yola, Z. Ustundag and L. Uzun, *Water Res.*, 2014, **48**, 210-217.

19. L. Han, X. Zhou, L. Wan, Y. Deng and S. Zhan, *J. Env. Chem. Eng.*, 2014, **2**, 123–130.

20. A. I. Borhan, P. Samoila, V. Hulea, A. R. Iordan and M. N. Palamaru, *J. Photoch. Photobio. A*, 2014, **279**, 17–23.

21. N. M. Mahmoodi, *Mater. Res. Bull*, 2013, **48**, 4255–4260.

22. J. Feng, L. Su, Y. Ma, C. Ren, Q. Gu and X. Chen, *Chem. Eng. J.*, 2013, **221**, 16-24.

23. A. Goyal, S. Bansal and S. Singhal, *Int. J. Hydrogen Energ.*, 2014, **39**, 4895-4905.

24. S. T. Hussain, S. R. Gilani, S. D. Ali and H. S. Bhatti, *J. Alloys Compd*., 2012, **544**, 99-104.

25. R. D. Waldron, *Phys. Rev*.,1955, **99**, 1727-1735.

26. W. B. White and W. A. De Angelis, *Spectrochim. Acta A*.,23, 1967, 985-995.

27. A. K. M. A. Hossain and M. L. Rahman, *J. Magn. Magn. Mater*., 2011, **323**, 1954-1962.

28. K. Krishna, K. V. Kumar and D. Ravinder, *Adv. Mater.Phy. Chem.*, 2012, **2**, 185-191.

29. R. Arulmurugan, B. Jeyadevan, G. Vaidyanathan and S. Sendhilnathan, *J.Magn.Magn.* Mater., 2005, **288**, 470-477.

30. S. Singhal, J. Singh, S. K. Barthwal and K. Chandra, *J. Solid State Chem*., 2005, 178, 3183-3189.

31. Y. Sun, G. Ji, M. Zheng, X. Chang, S. Lib and Y. Zhang, *J. Mater. Chem*., 2010, **20**, 945-952.

32. J. Kreisel, G. Lucazeau and H. Vincent, *J. Solid State Chem*.,1998, **137**, 127-137.

33. G. Pandey and S. Dixit, *J. Phys. Chem. C*, 2011, 115, 17633-17642.

34. X. Li, Y. Hou, Q. Zhao and L. Wang, *J. Colloid and Interface Sci*., 2011, **358**, 102-108.

35. K. Esumi, K. Miyamoto and T. Yoshimura, *J. Colloid Interface Sci*., 2002, **254**, 402 -405.

36. K. Hayakawa, T. Yoshimura and K. Esumi, *Langmuir*., 2003, **19**, 5517 –5521.

37. Y. Lu, Y. Mei, M. Drechsler and M. Ballauff, *Angew. Chem*., 2006, **118**, 827 – 830.

38. J. Lee, J. C. Park and H. Song, *Adv. Mater*., 2008, **20**, 1523 – 1528.

39. X. Du, J. He, J. Zhu, L. Sun and S. An, *Appl. Surf. Sci*., 2012, **258**, 2717-2723.

40. L. Ai, H. Yue and J. Jiang, *J. Mater. Chem*., 2012, **22**, 23447-23453.

41. S. U. Nandanwar and M. Chakraborty, *Chin. J. Catal*., 2012, **33**,1532-1541

42. E. Casbeer, V. K. Sharma, X. Z. Li, *Sep. Purifi. Techno*., 2012, **87**, 1-14.

Table 1. Crystallite size of $Ni_xCo_{1-x}Fe_2O_4$ with different concentration of Ni^{2+} ions.

Sample name	Lattice parameter a(Å)	Average Crystallite size (nm)	X-ray density (g/cm^3)
$CoFe_2O_4$	8.382	5.4	5.29
$Ni_{0.2}Co_{0.8}Fe_2O_4$	8.379	4.8	5.31
$Ni_{0.4}Co_{0.6}Fe_2O_4$	8.372	6.0	5.35
$Ni_{0.6}Co_{0.4}Fe_2O_4$	8.365	4.7	5.29
$Ni_{0.8}Co_{0.2}Fe_2O_4$	8.351	4.6	5.30
$NiFe_2O_4$	8.332	4.1	5.38

Table 2. Completion time for the reduction of 4-NP using different mol% of $Ni_xCo_{1-x}Fe_2O_4$ (x = 0.0, 0.2, 0.4, 0.6, 0.8 and 1.0) nanoparticles with 50 and 25 equivalents of $NaBH_4$.

Catalyst	5 mol%	10 mol%	30 mol%	30 mol%
	$NaBH_4$ (50 equivalents)			$NaBH_4$ (25 equivalents)
	Completion time (min)			
$CoFe_2O_4$	No reaction	No reaction	No Reaction	No Reaction
$Ni_{0.2}Co_{0.8}Fe_2O_4$	55	25	6	40
$Ni_{0.4}Co_{0.6}Fe_2O_4$	15	15	2	30
$Ni_{0.6}Co_{0.4}Fe_2O_4$	5	2	0.5	20
$Ni_{0.8}Co_{0.2}Fe_2O_4$	12	2.5	2	40
$NiFe_2O_4$	5	3	0.5	45

Table 3. Apparent rate constant values for the reduction of 4-NP using different mol% of $Ni_xCo_{1-x}Fe_2O_4$(x = 0.0, 0.2, 0.4, 0.6, 0.8 and 1.0) nanoparticles with 50 and 25 equivalents of $NaBH_4$.

Catalyst	5 mol%	10 mol%	30 mol%	30 mol%
	$NaBH_4$ (50 equivalents)			$NaBH_4$ (25 equivalents)
	Apparent rate constant (K_{aap}) min^{-1}			
$CoFe_2O_4$	No reaction	No reaction	No Reaction	No Reaction
$Ni_{0.2}Co_{0.8}Fe_2O_4$	0.061	0.167	1.179	1.050
$Ni_{0.4}Co_{0.6}Fe_2O_4$	0.350	0.207	3.819	0.092
$Ni_{0.6}Co_{0.4}Fe_2O_4$	1.107	2.437	10.328	0.268
$Ni_{0.8}Co_{0.2}Fe_2O_4$	0.275	2.032	2.062	0.121
$NiFe_2O_4$	0.873	1.605	9.965	0.139

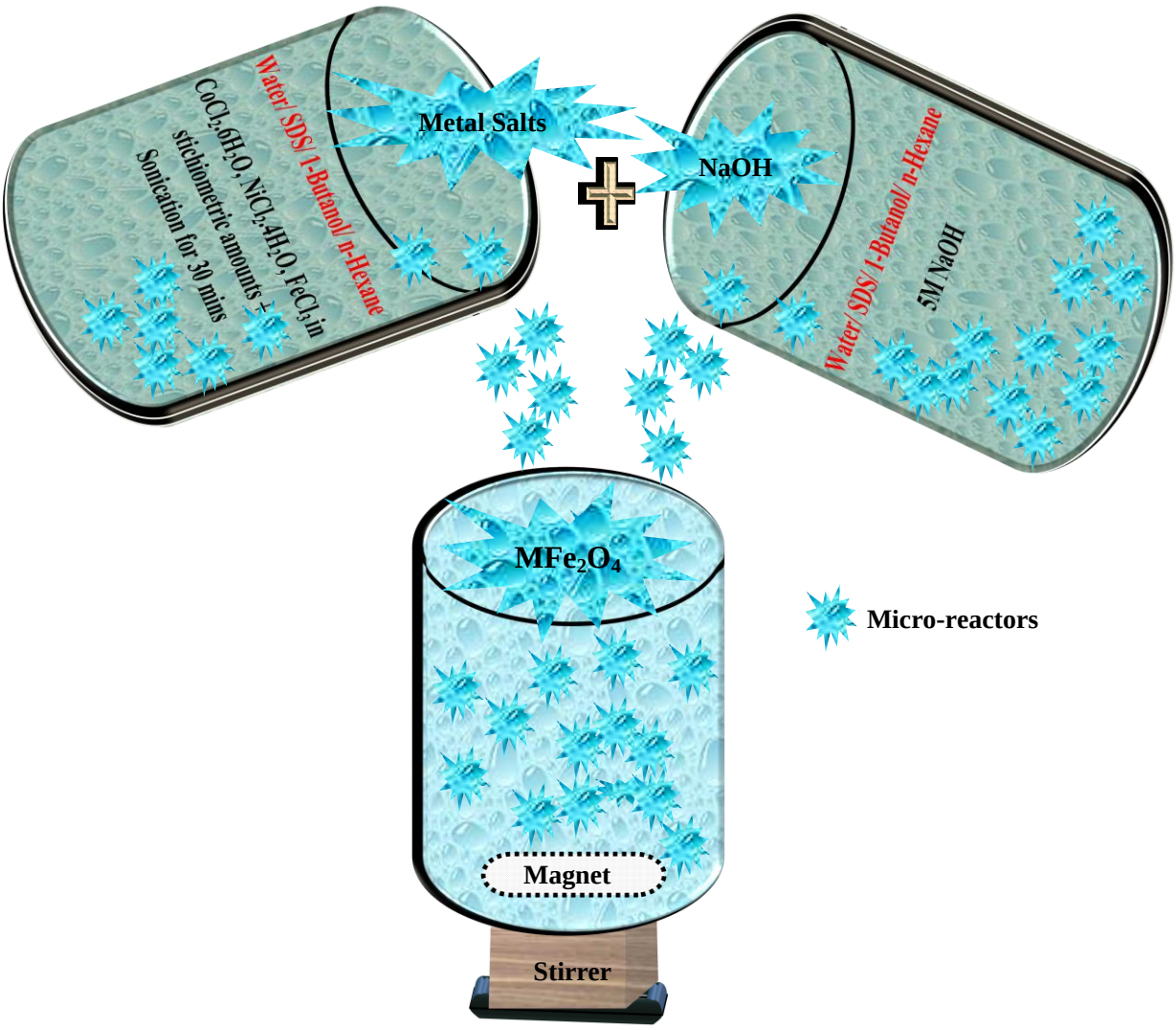

Fig 1. Schematic diagram for the synthesis of Nickel doped Cobalt Ferrite by Microemulsion Method.

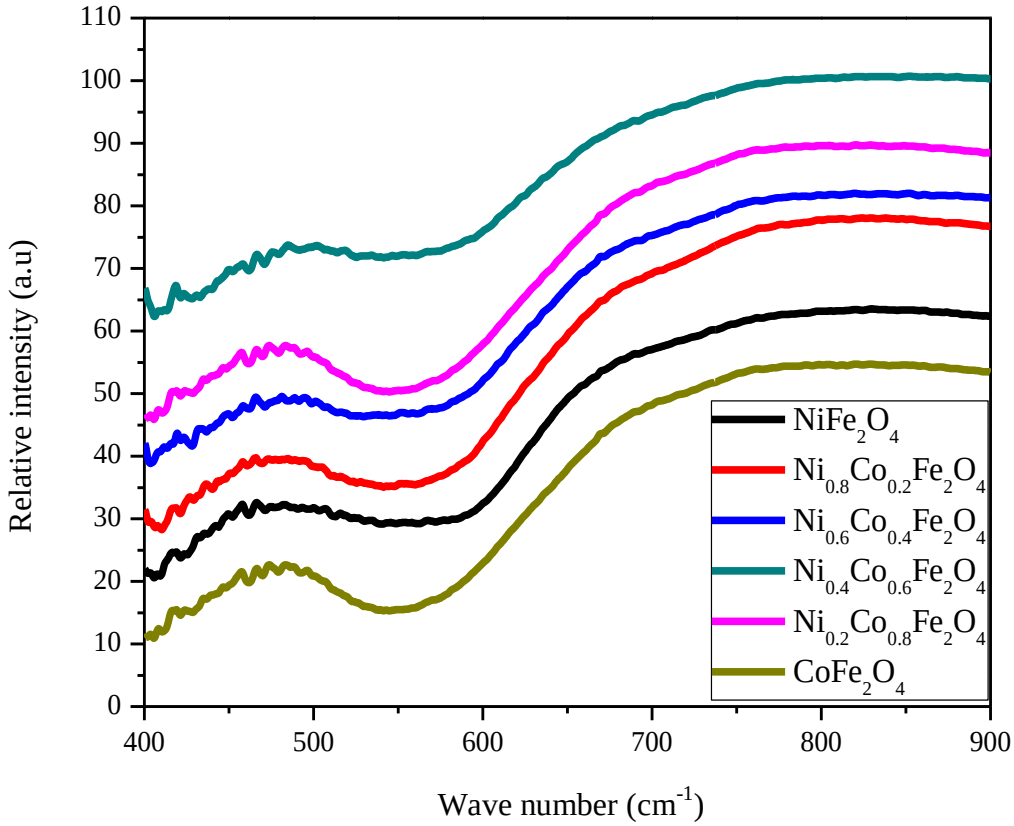

Fig 2. FT-IR spectra of nickel doped cobalt ferrite nanoparticles.

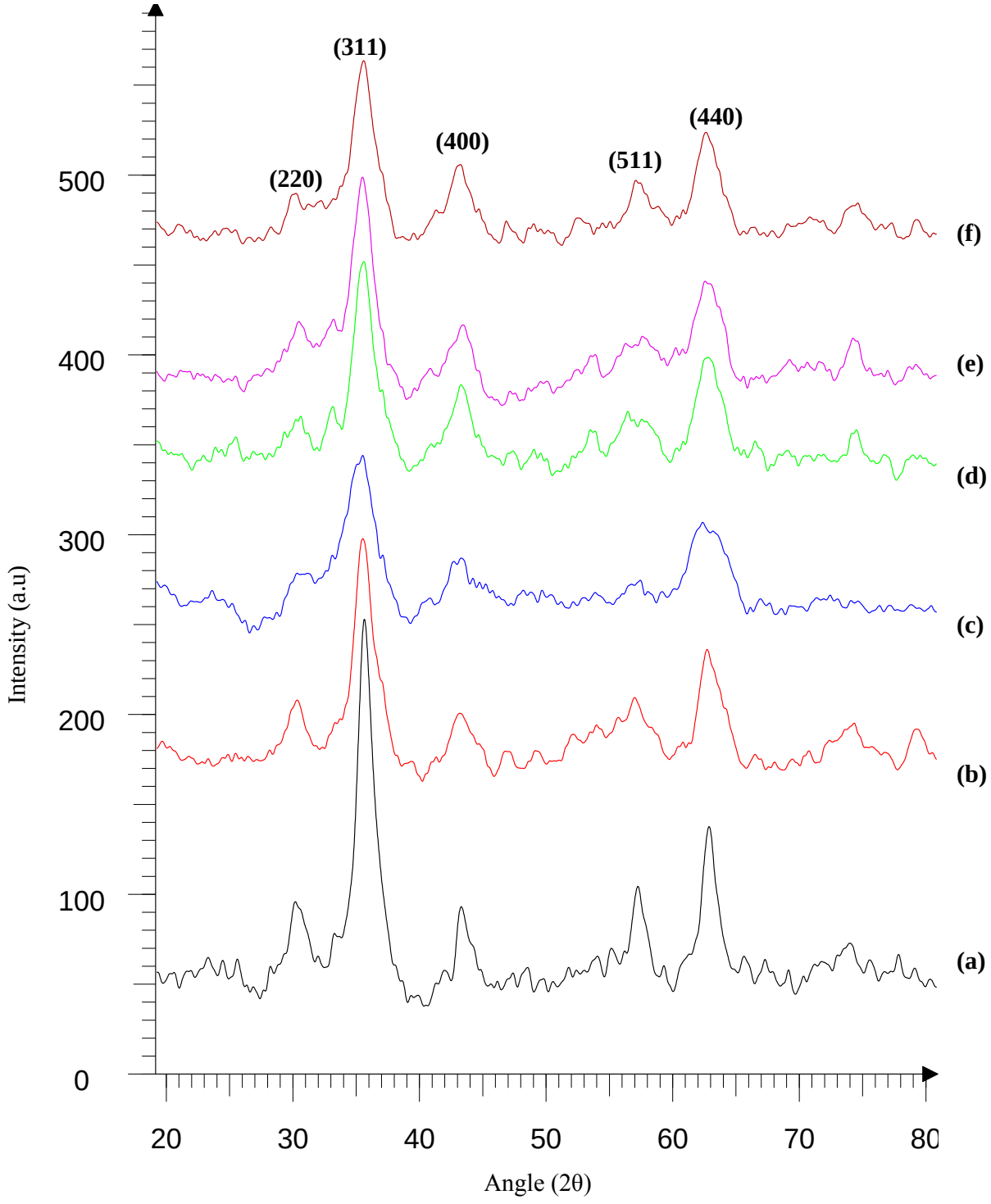

Fig 3. XRD pattern of nickel doped cobalt ferrite ($Ni_xCo_{1-x}Fe_2O_4$) where (a) x=0.0, (b) x=0.2, (c) x=0.4, (d) x= 0.6, (e) x=0.8 and (f) x=1.0

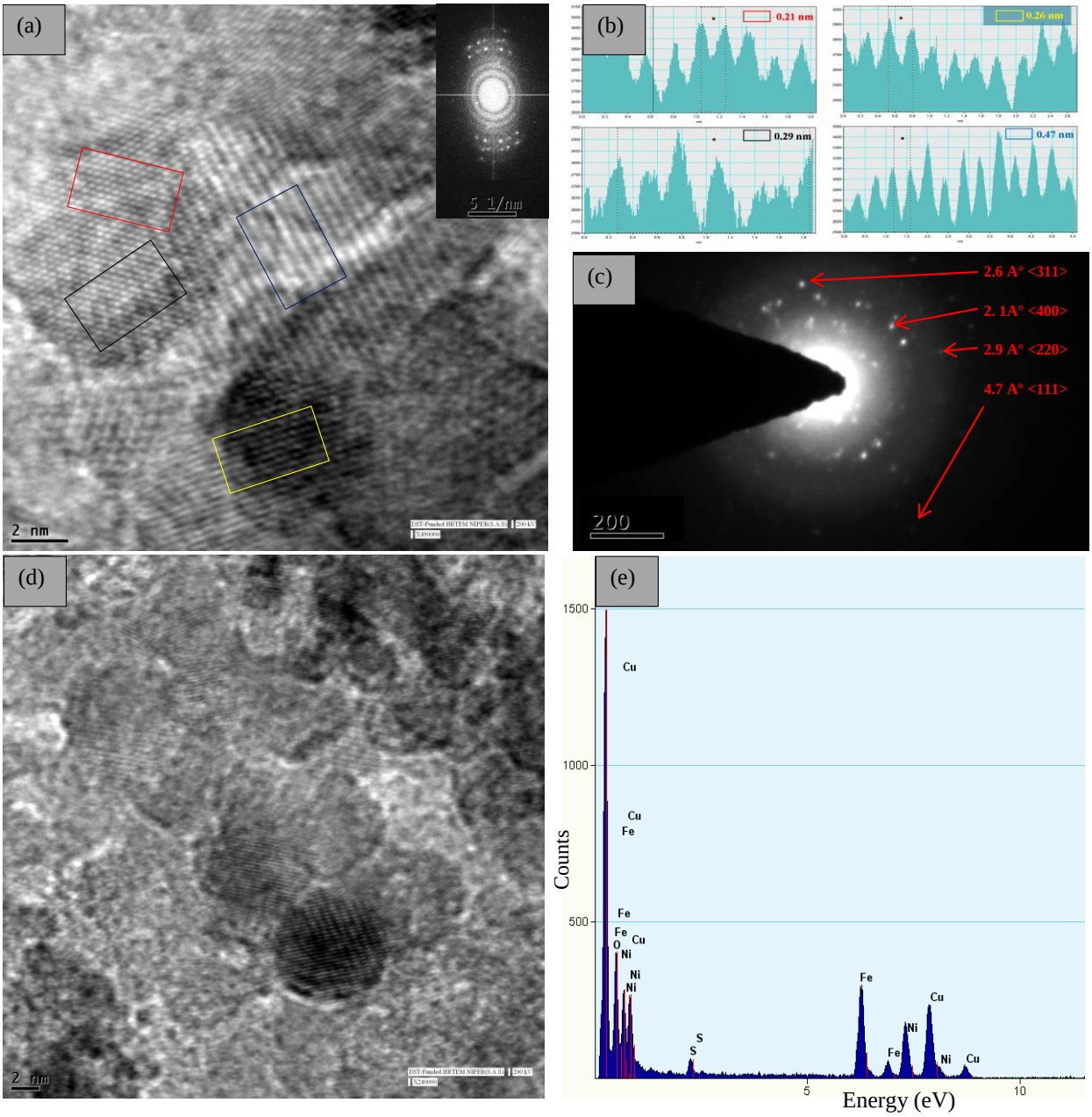

Fig 4. HRTEM image of $NiFe_2O_4$ nanoparticles showing (a) lattice interplaner distance and inset showing the FFT of nickel ferrite (b) profile of frame for the average fringe width at different portions of image (c) SAED pattern (d) Spherical nanoparticles at 2 nm resolution and (e) Energy Dispersive X-ray spectra.

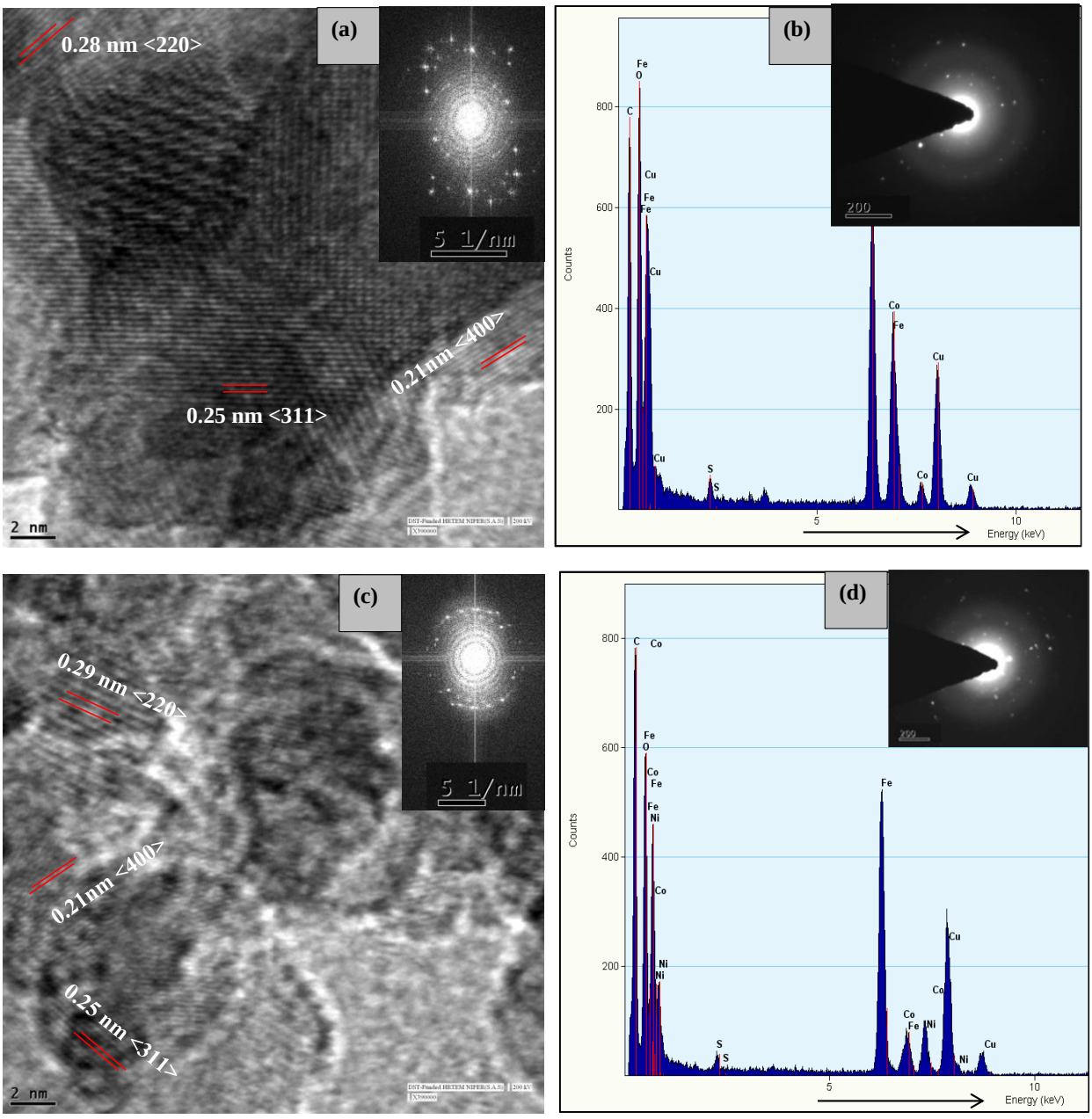

Fig 5. HRTEM image of (a) $CoFe_2O_4$ nanoparticles showing lattice interplaner distance and inset showing the FFT of ferrite (b) Energy Dispersive X-ray spectra and inset showing the SAED Pattern of cobalt ferrite nanoparticles (c) $Co_{0.4}Ni_{0.6}Fe_2O_4$ nanoparticles fringe width (d) Energy Dispersive X-ray spectra and inset having SAED pattern of $Co_{0.4}Ni_{0.6}Fe_2O_4$ nanoparticles.

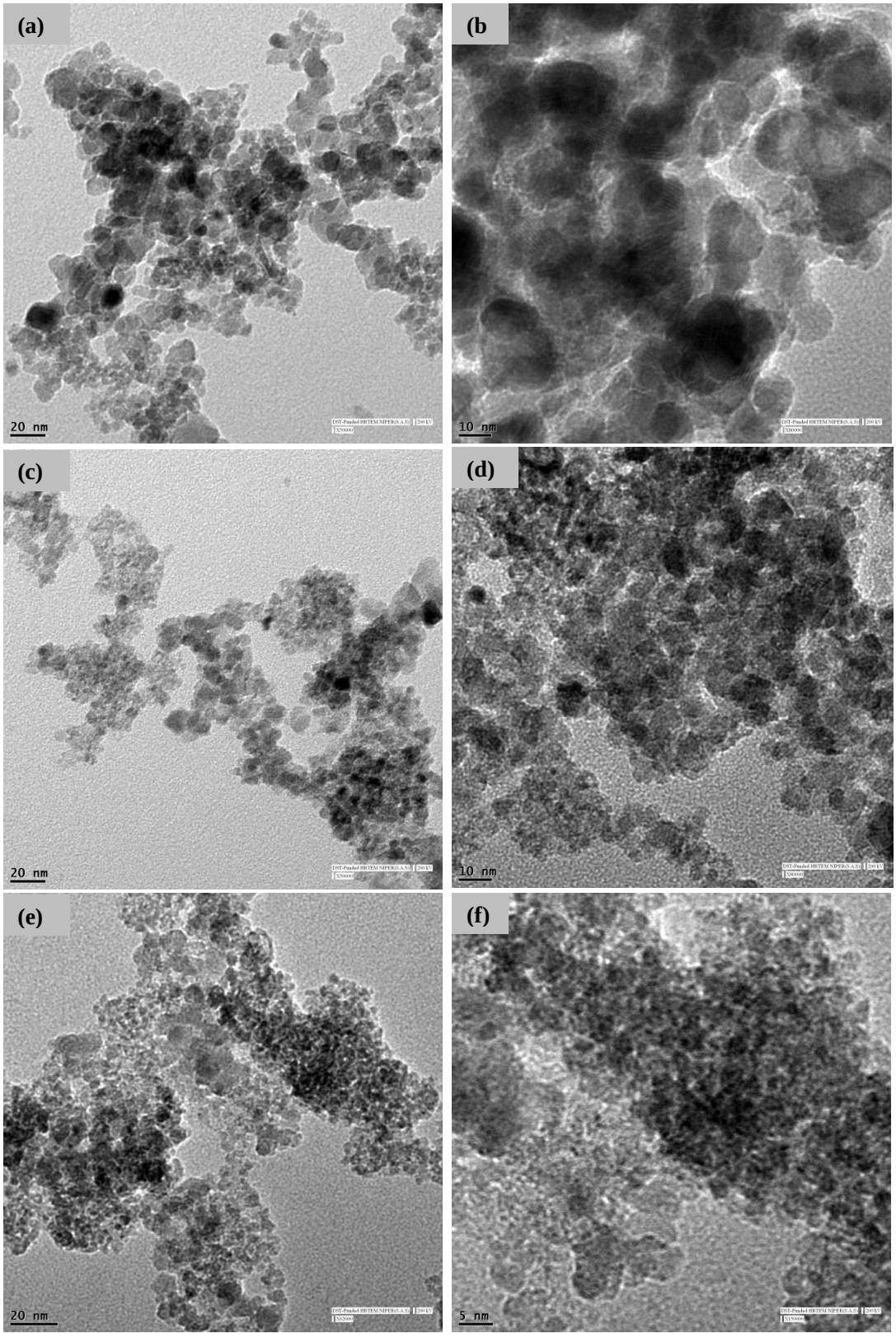

Fig 6. TEM Images of (a, b) $CoFe_2O_4$ (c, d) $Co_{0.4}Ni_{0.6}Fe_2O_4$ and (e, f) $NiFe_2O_4$ nanoparticles.

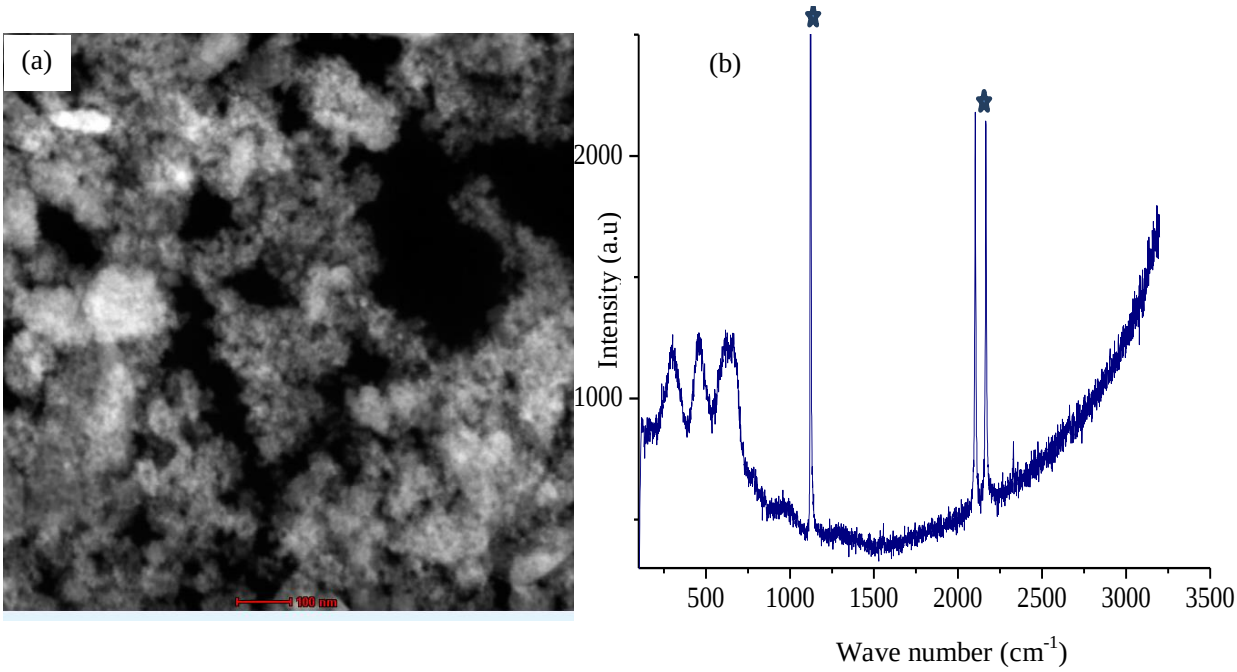

Fig 7. $Ni_{0.6}Co_{0.4}Fe_2O_4$nanoparticles (a) STM image showing the particle morphology (b) Raman spectra (Peaks marked as asterisk correspond to the back ground radiation of the instrument).

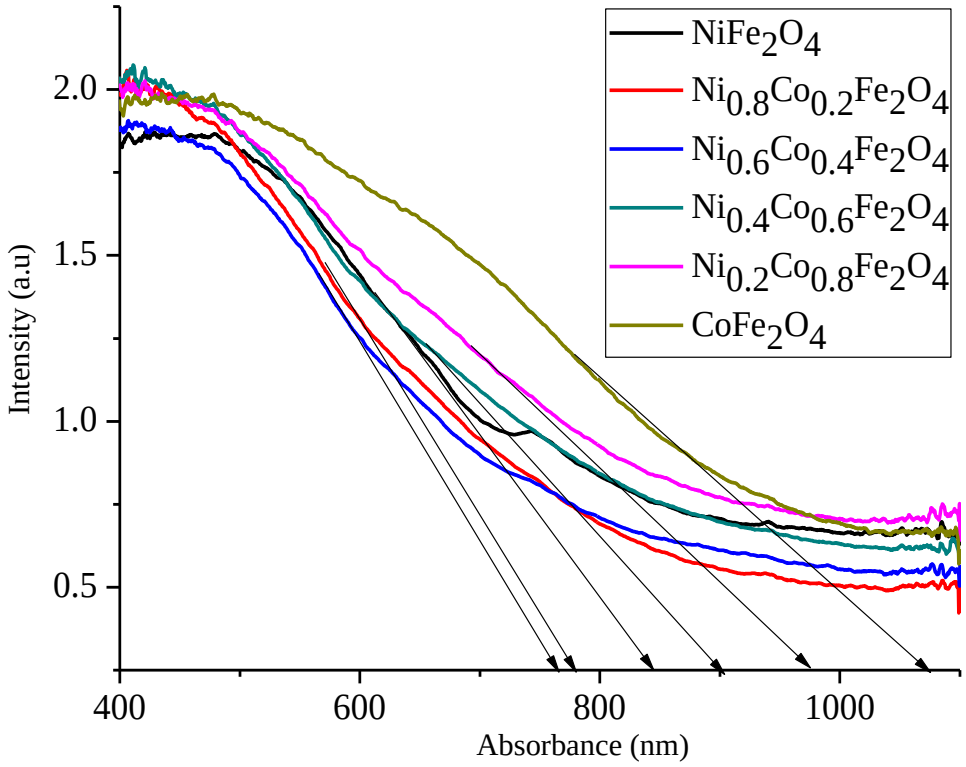

Fig 8. Diffused UV–Visible spectra of $Ni_xCo_{1-x}Fe_2O_4$ nanoparticles with varying Ni^{2+} dopant showing different band edge absorbance annealed at 400 °C for 5h

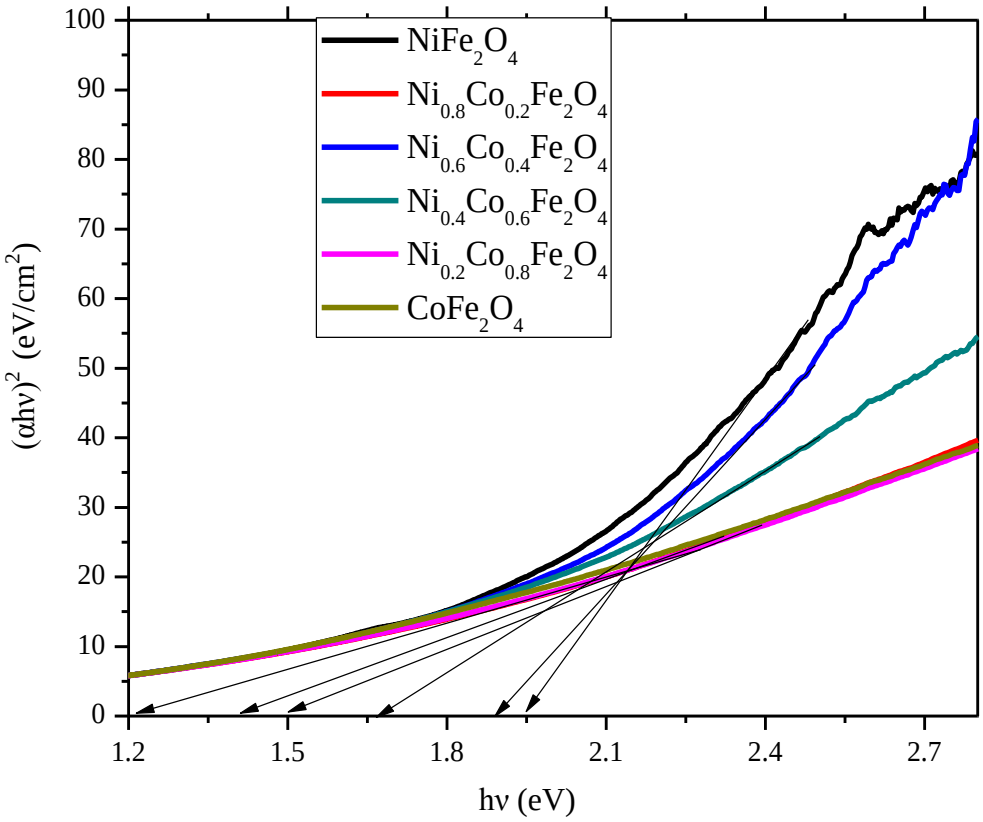

Fig 9. Plots of $(\alpha h\nu)^2$ versus $h\nu$ showing the band gap of $Ni_xCo_{1-x}Fe_2O_4$ nanoparticles with variable Ni^{2+} ion doping in cobalt ferrite nanoparticles

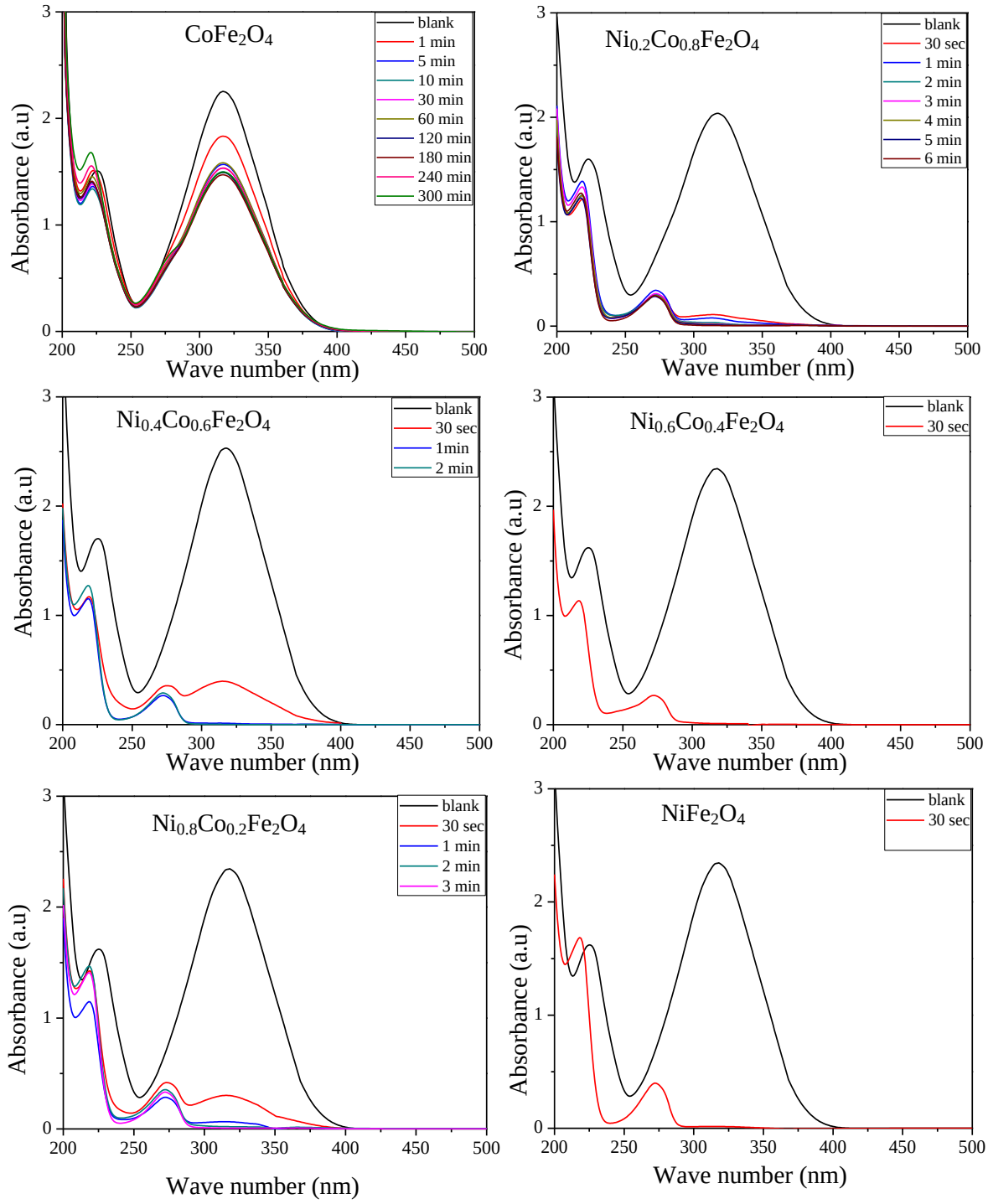

Fig 10. UV-Visible spectra showing the reduction of 4-NP with 50 equivalents of $NaBH_4$ catalyzed using 30 mol% of $Ni_xCo_{1-x}Fe_2O_4$ (a) x = 0.0, (b) x = 0.2, (c) x = 0.4, (d) x = 0.6, (e) x = 0.8 and (f) x = 1.0

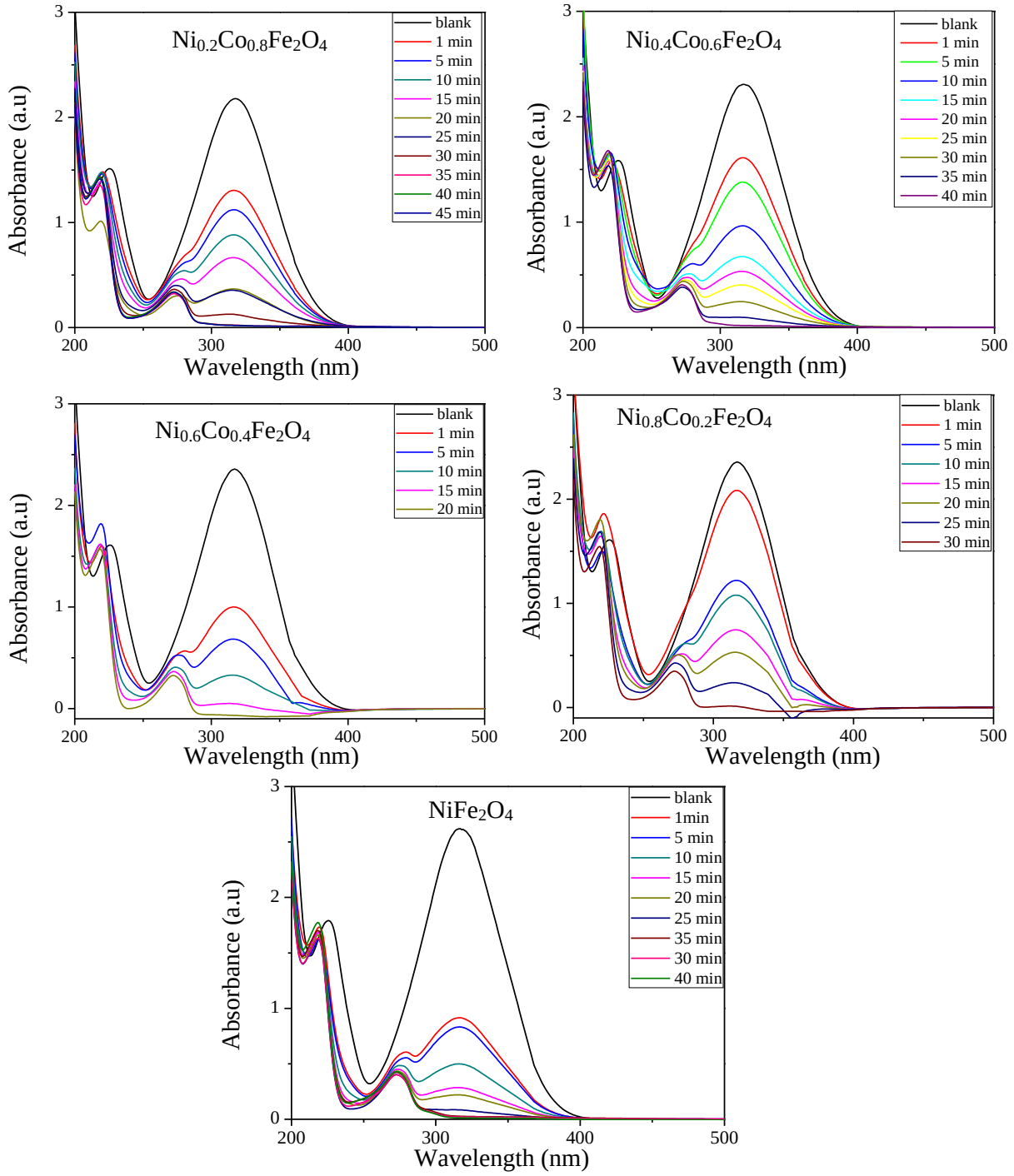

Fig 11. UV-Visible spectra showing the reduction of 4-NP with 25 equivalents of $NaBH_4$ catalyzed using 30 mol% of $Ni_xCo_{1-x}Fe_2O_4$ (a) x = 0.0, (b) x = 0.2, (c) x = 0.4, (d) x = 0.6, (e) x = 0.8 and (f) x = 1.0

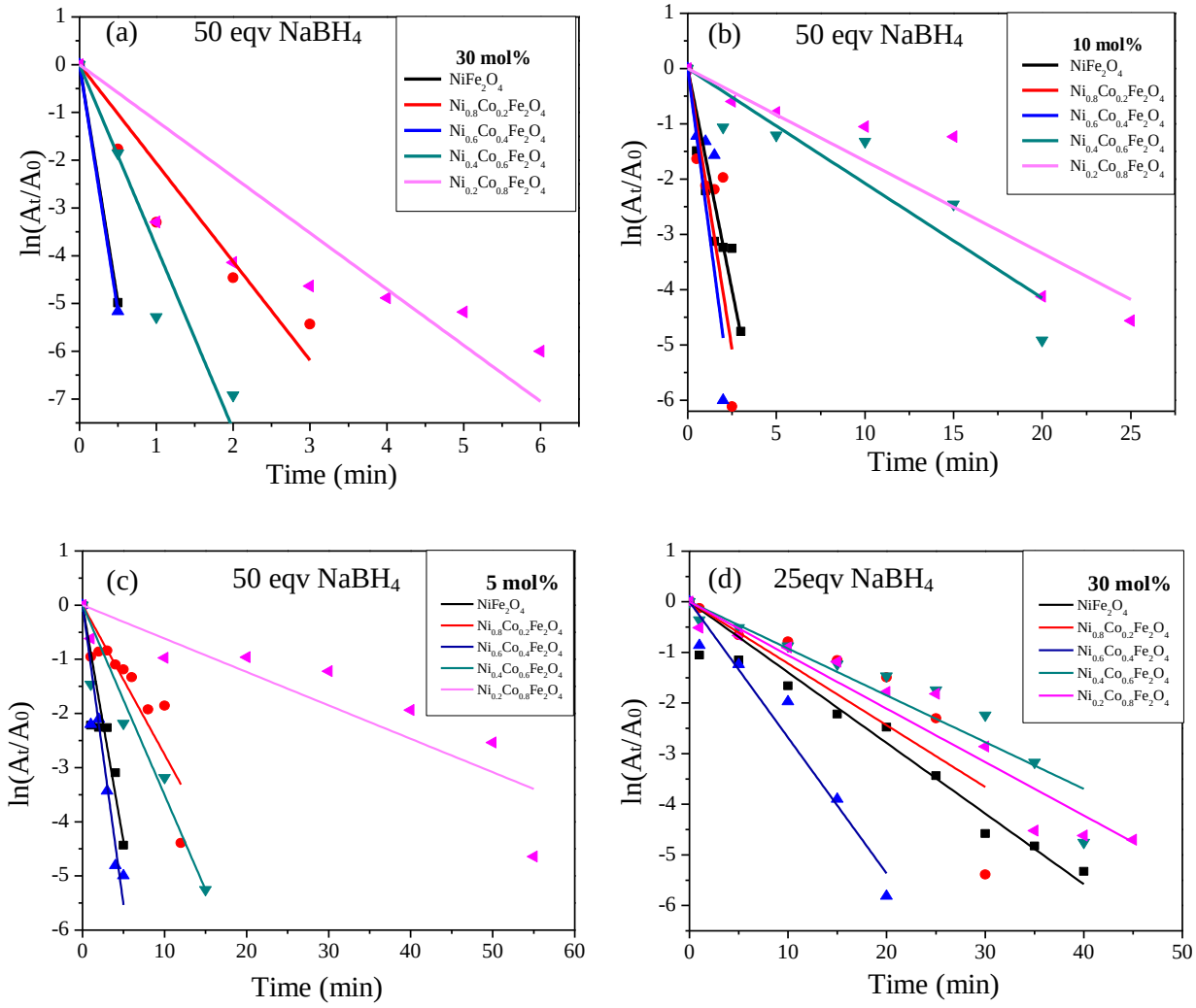

Fig 12. Plots of $\ln(A_t/A_0)$ vs time for the reduction of 4-NP using 50 eqv $NaBH_4$ in the presence of (a) 30 mol% (b) 10 mol% (c) 5 mol% $Ni_xCo_{1-x}Fe_2O_4$ nanoparticles and (d) 25 eqv $NaBH_4$ in presence of 30 mol% $Ni_xCo_{1-x}Fe_2O_4$ nanoparticles.

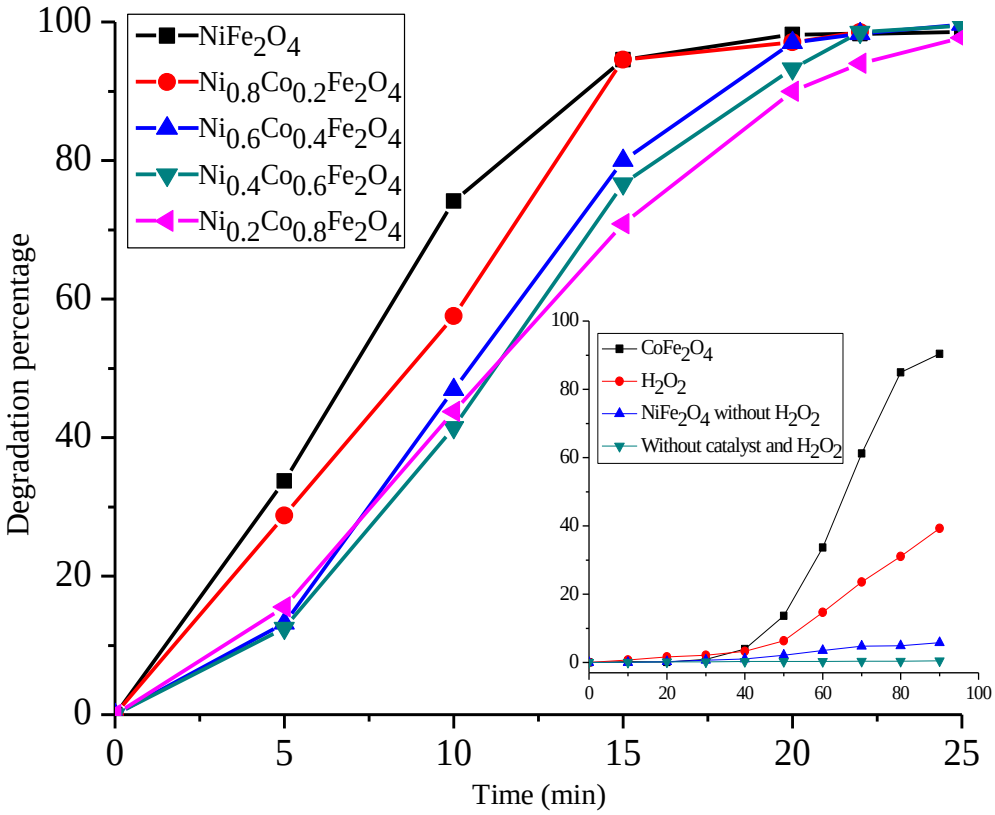

Fig 13. Degradation percentage of 50 µM rhodamine B dye over the time using 50 mg of nickel cobalt ferrite nanoparticles and 100 µL of 30% H_2O_2 at a pH of 2 (inset showing the degradation percentage of rhodamine B using $CoFe_2O_4$, H_2O_2, $NiFe_2O_4$ without H_2O_2 and light in the absence of catalyst and H_2O_2)